

# Analysis of GSI HADES beamline configuration space

Mariusz Sapinski\*

GSI Helmholtzzentrum für Schwerionenforschung, Darmstadt, Germany

Dominik Vilsmeier,

Goethe Universität Frankfurt, Frankfurt, Germany

February 12, 2020

## Abstract

The High-Energy Beam Transport system of GSI Campus is a complex system of interconnected beamlines between SIS18 synchrotron and multiple experimental stations and storage rings. This system is designed to be flexible and each experimental station can be reached by several beam paths. The quadrupole settings must fulfill constraints due to the beamline acceptance, limitations of the installed magnets and experimental requirements. The number of degrees of freedom is large and leaves operators with a vast number of possible optics configurations. The choice of a particular configuration is often a matter of compromises, very specific requirements, operational experience and personal style. Once a satisfying configuration is found, the space of possible solutions is usually not explored any further. Here the Monte Carlo method is used to probe the space of all possible beamline optics configurations. The focus is on a particular section, the HADES beamline, because this is one of the most demanding lines due to high beam intensities required by the experiment. The presented analysis gives an overview of the possible settings, insight into beamline potential and flexibility and supports the choice of an optimal operational setting.

---

\*m.sapinski@gsi.de

# 1 Introduction

A transfer line is a part of an accelerator facility without accelerating cavities, used to transport the beam between accelerators or from an accelerator to experiments. The main constituents of a beamline are dipoles, quadrupoles and steerer magnets. Other types of magnets are rarely used. Dipole settings are defined by the geometry of the beamline. Quadrupoles, together with beam properties at the entrance of the beamline, define what is called *beam optics*.

In GSI, the network of beamlines starting at SIS18 heavy ion synchrotron is called HEST (from German "Hochenergie-Strahlführung") [1]. The beamlines bifurcate, cross and reunite in a particular, complex pattern adapted to the experiments. HADES [2] is one of the largest experiments and it is placed at the end of an about 160 meter long beamline starting at the magnetic septum of SIS18. The beamline contains 21 individually powered quadrupoles and two active dipoles tilted by  $21.7^\circ$  to bring the beam to the elevated position of the experimental area [3, 4]. HADES is designed to work in two main modes, using either primary or secondary particles. Here the first case is studied, in which the beam is focused on an internal target inside the experiment. In both cases HADES accepts slowly extracted beams which are realized by incrementally changing the tune towards third order resonance. The required beam spot size is about  $\sigma = 0.4$  mm [5]. Only about 1% of ions interact with the target and the rest of the beam is dumped downstream of the experiment. A typical ion optics used in operation, called *BEAMTIME2019*, is visualized in Figure 1.

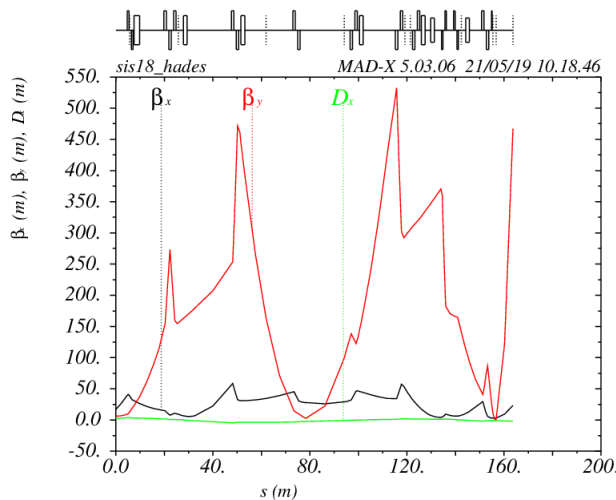


Figure 1: Example of ion optics for HADES beamline used during the beam time in 2019. The experimental target is located at 158 m.

Setting up a beamline optics involves fulfillment of various constraints. Typically the beam should be transported with maximum transmission and focused on the experimental target. These constraints can be fulfilled by various quadrupole config-

urations. Therefore, an analysis of the set of all possible configurations can provide interesting insights about the beamline capabilities.

The relevant configuration space has 21 dimensions corresponding to the 21 quadrupoles. Because of its high dimensionality the volume of this space is extremely large and thus it is not possible to generate and compute all possible configurations. A randomly sampled subset of configurations can however be chosen in order to represent the full population.

This paper is structured as follows: in Section 2 the probing of configuration space and generation of data sets is described, in Section 3 the general properties of optics functions are discussed, in Section 4 the configuration space is analyzed and in Section 5 the potential for dimensionality reduction is investigated. In Section 6 the microstructure of the configuration space is investigated. Section 7 presents Principal Component Analysis of the  $k_1$ -values. In Section 8 a grouping of configurations is discussed. Section 9 discusses stability of the optics, considering quadrupoles gradient errors as well as a shifting of Twiss parameters at the entrance of the beamline. Finally, the last Section contains a discussion on the choices of the operational ion optics in view of previous results.

## 2 Samples

Three data sets with 10 000 configurations each have been generated. They use randomly sampled  $k_1$ -values for the 21 quadrupoles which are used as starting points for a subsequent MADX [7] matching procedure.

The three data sets differ in the matching constraints on the beta function which are described in Table 1. In addition to these constraints the  $\beta_{h,v}$  on the beam dump, downstream of the experimental target, is constrained to less than 3000 m. The Levenberg-Marquardt algorithm [8], which is implemented as *LMDIF* in MADX, is used as the matching method with the maximum number of function evaluations set to  $1 \times 10^7$  and a tolerance of  $1 \times 10^{-16}$ . Only 0.03 % of the randomly chosen starting points converged during the matching procedure. Table 2 contains an overview of the various termination reasons of the LMDIF algorithm. The data sets contain only successfully converged configurations for the further analysis. The further analysis is concentrated around the  $\mathcal{D}_{1.0}^{500}$  data set.

Table 1: Summary of data sets and associated matching constraints.

data set	Constraints	
	beamline	target
$\mathcal{D}_{1.0}^{500}$	$\beta_{h,v} < 500$ m	$\beta_{h,v} < 1.0$ m
$\mathcal{D}_{0.2}^{500}$	$\beta_{h,v} < 500$ m	$\beta_{h,v} < 0.2$ m
$\mathcal{D}_{1.0}^{250}$	$\beta_{h,v} < 250$ m	$\beta_{h,v} < 1.0$ m

Table 2: Overview of the various LMDIF termination reasons that occurred during probing of the configuration space. Here "unstable" means that the six-dimensional orbit vector grew too large along the beamline during the matching process.

Reason	Fraction
unstable	93.8370 %
converged without success	3.2336 %
variables too close to limit	2.8957 %
converged successfully	0.0336 %
call limit	0.0002 %

The matching constraints lead to strong limitations and interrelations with respect to the  $k_1$ -values. The results of the matching procedure depend not only on the matching conditions but also on the used algorithm. The Levenberg-Marquardt minimization uses gradient descent and it stops as soon as all constraints are fulfilled. Thus it is possible that a given result could be further optimized towards even smaller values of the beta function but this possibility is not explored by the optimizer.

### 3 Optics properties

The minimization procedure stops as soon as all constraints are fulfilled, including cases where some of the constrained quantities end up well below their associated thresholds. This becomes apparent on the left plot of Figure 2, where a large number of configurations clearly surpass their constraints. Imposing stronger constraints results in a smaller possible margin and the constrained quantities remain closer to their threshold values, as can be seen from the right plot of Figure 2. This suggests that the constraints of the  $\mathcal{D}_{0.2}^{500}$  case are close to the limits of the beamline.

The dispersion at the target is a relevant property of the optics as well which however was not constrained during the matching process. Vertical dispersion is small but non-zero due to the presence of tilted dipoles. Small horizontal dispersion is desirable because the beam momentum changes during the spill resulting in potential movement of the beam spot on target. In order to counteract this movement, the first steering dipoles after the extraction septum can be ramped during the spill and therefore zero dispersion at the target is not absolutely necessary but desirable nonetheless.

The distribution of dispersion at the target is shown on the left plot of Figure 3. The right plot of this figure presents another interesting aspect of the minimization procedure. The phase advance on the target tends to prefer values corresponding to certain angles (or 180-degree rotations). For instance the peaks for vertical phase advance are located around  $\pi$ ,  $1.5\pi$  and  $2\pi$  for  $\mathcal{D}_{0.2}^{500}$ . For other data sets, the peaks are less pronounced. This shows that the whole beamline must be more precisely

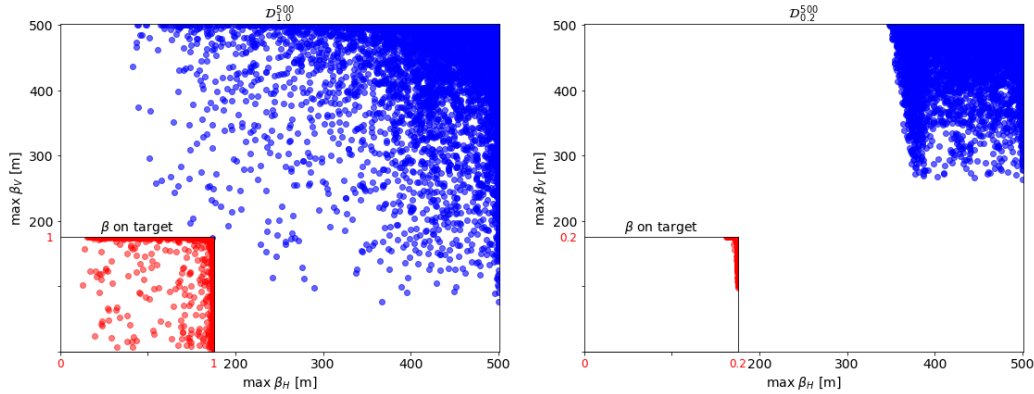


Figure 2: Values of the final beta function along the beamline (maximum value, blue) and at the target location (red) for  $\mathcal{D}_{1.0}^{500}$  (left) and  $\mathcal{D}_{0.2}^{500}$  (right).

tuned when a stronger constraint on the target focusing is imposed.

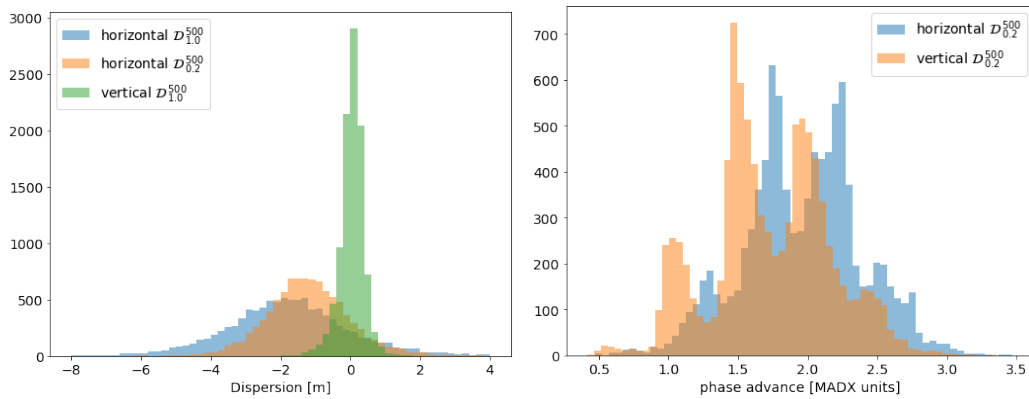


Figure 3: Left: Distribution of horizontal and vertical dispersion on the target. Right: Distributions of the phase advance on the target plotted for  $\mathcal{D}_{0.2}^{500}$  sample; for  $\mathcal{D}_{1.0}^{500}$  a similar structure occurs but the peaks are less pronounced.

## 4 Configuration space

The configuration space spans across 21 dimensions defined by  $k_1$ -values of the quadrupole magnets. The beamline contains two types of quadrupole magnets and their main properties are shown in Table 3.

The configuration space is a 21-orthotope with 2 097 152 vertices. The corresponding volume is

$$V_{21} = \prod_{i=1}^{21} \max |k_{1,i}| = 1.21 \times 10^{-6} \text{ m}^{-42} \quad (1)$$

Table 3: Quadrupole types installed on the beamline.

Type	Length	max $ k_1 $	Count
QPK	0.6 m	0.37 m <sup>-2</sup>	6
QPL	1.0 m	0.60 m <sup>-2</sup>	15

The notion of volume in 21 dimensions is far from being intuitive and probably a better grasp is provided by the largest one-dimensional span between the edges of the configuration space. This maximum Euclidean distance is 2.49 m<sup>-2</sup>.

The available configuration space is strongly reduced by the constraints listed in Table 1. The distribution of resulting  $k_1$ -values is approximately continuous and it does not peak at the extremes of  $k_1$ -values, as shown, for a selection of magnets, on the left plot of Figure 4. Therefore, the volume occupied by the converged configurations can be estimated from eigenvalues ( $\lambda_i$ ) of the covariance matrix using equation 2. The eigenvalues of the covariance matrix represent the variances of the projection of the 21-dimensional distribution onto the eigenvectors. If these distributions are Gaussian, then width of the distribution  $\sigma_{gauss} = \sqrt{\lambda}$ . The distributions are not always Gaussian, especially for the eigenvectors with largest variance (see Section 7), so the proposed estimation is an approximation. For non-Gaussian distributions Chebyshev's inequality can be used to estimate which percentage of configurations lie within a given range of variances, i.e. in the range  $\pm 2\sqrt{\lambda}$  there should be between 75% (Chebyshev's inequality) and 95% (normal distribution) of configurations. In addition, due to presence of substructures in the configuration space, this approach overestimates the actual space of valid parameters. This will be discussed further in Section 6.

$$V_{21} = 4^{21} \prod_{i=1}^{21} \sqrt{\lambda_i} \quad (2)$$

The covariance matrix is visualized on the right plot of Figure 4. The quadrupole triplet and two doublets with largest values of matrix elements constitute the first two principal components (see Section 7).

The volume of the configuration space which contains matched configurations is about 10<sup>-4</sup> of the total volume. As one can see from Table 4, constraining the beamline beta function by factor 2 (from 500 m to 250 m) decreases the configuration space volume by factor 10 and constraining the beta function on the target by factor 5 decreases the configuration space volume by factor 50.

The distribution of distances between initial and final configurations and distances to the closest and the most distant configuration are shown in Figure 5. The average distance to the closest configuration before the matching procedure is 0.41 m<sup>-2</sup> and drops to 0.29 m<sup>-2</sup> for the converged configurations. This distance is never zero, the models do not overlap. The average distance between corresponding initial and final configurations is 0.46 m<sup>-2</sup> which is significantly larger than the

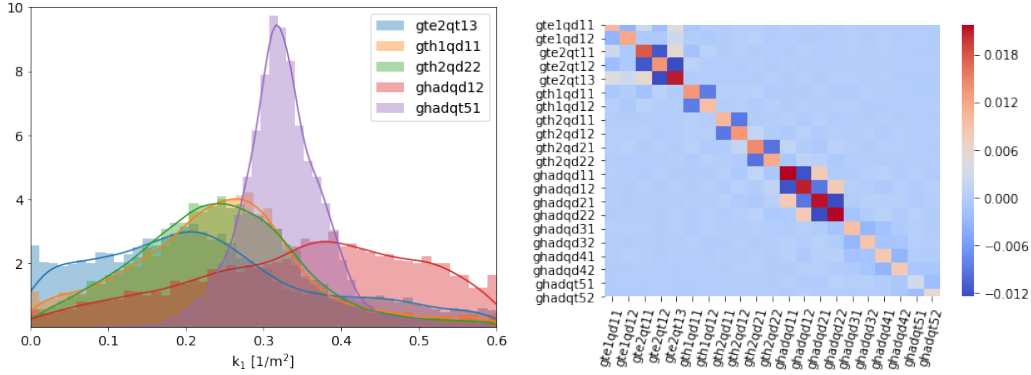


Figure 4: Left: distribution of selected  $k_1$ -values selected as examples. Right: covariance matrix for the  $k_1$ -values. The correlations between the quadrupole doublets are observed.

Table 4: Configuration space volume calculated with Equation 2.

sample	Volume [ $\text{m}^{-42}$ ]
$\mathcal{D}_{1.0}^{500}$	$7.93 \cdot 10^{-10}$
$\mathcal{D}_{1.0}^{250}$	$6.29 \cdot 10^{-11}$
$\mathcal{D}_{0.2}^{500}$	$1.29 \cdot 10^{-11}$

distance to the final nearest neighbour. The maximum stretch of the reduced configuration space is only  $1.51 \text{ m}^{-2}$ .

The last characteristic length is related to the local size of a configuration, which will be discussed in more detail in Section 6. It describes the local region which fulfills the matching conditions. Due to the high dimensionality of the problem, the precise shape of this region is difficult to estimate. An increase of sampling requires enormous computing power, not available for this study.

Two approaches are used in this study. In the first approach small, selected areas of the configuration space are sampled with very large granularity. In the second approach, for each configuration a set of 42 variations is created. For each variation one of the  $k_1$ -values is changed by  $\pm r_{21}$ .

The left plot of Figure 6 shows the distribution of mean and maximum values of  $\beta/\beta_0$  ratio on target for  $r_{21} = 0.002 \text{ m}^{-2}$ . The right plot shows the evolution of the  $\beta/\beta_0$  as a function of investigated distance  $r_{21}$  from the original configuration. From this analysis we can conclude that the typical size of a configuration space occupied by a configuration is about  $0.002 \text{ m}^{-2}$  to  $0.005 \text{ m}^{-2}$ , however closer analysis reveals much larger structures.

The various characteristic lengths are summarized Table 5.

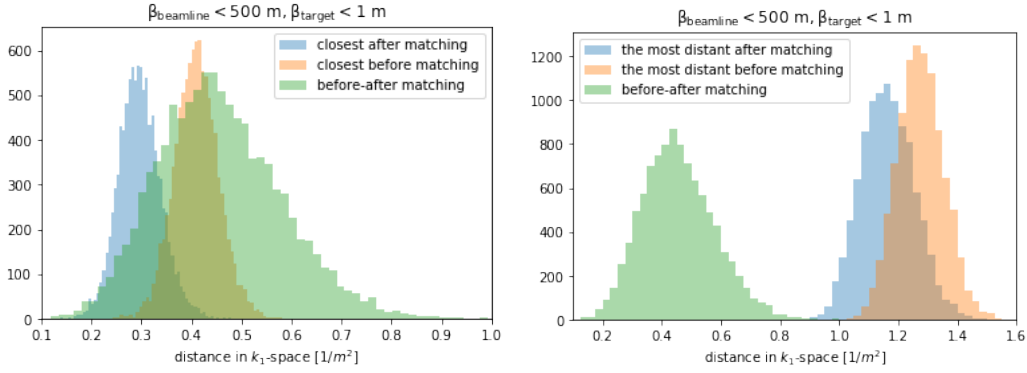


Figure 5: Left: distribution of minimum distances between configurations. Right: distribution of maximum distances between configurations.

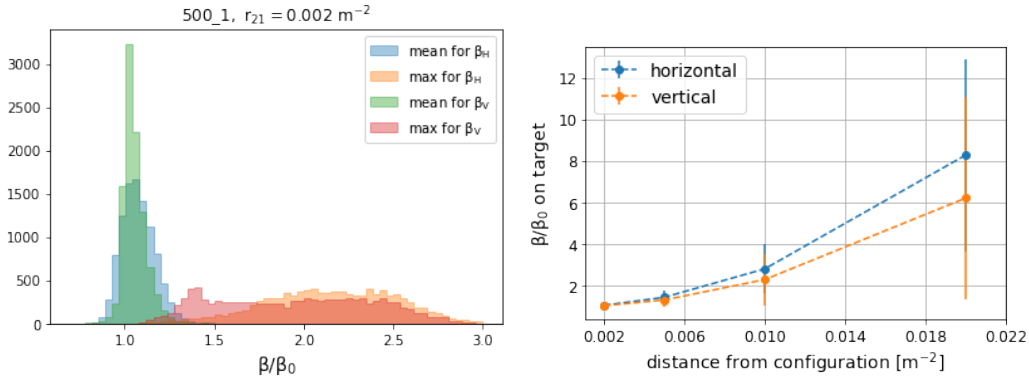


Figure 6: Left plot: Average and maximum change of the  $\beta$  function on target for configurations in a distance of  $0.002 \text{ m}^{-2}$  from the configurations found by the minimization procedure. Right plot: mean value of  $\beta/\beta_0$  for various  $r_{21}$ .

Table 5: Overview of various characteristic lengths (measured as Euclidean distances). "fn" stands for "farthest neighbor" and "nn" stands for "nearest neighbor" in configuration space. "initial-final" denotes the distance of corresponding initial and final configuration pairs. Distances are given in units of  $\text{m}^{-2}$ .

	mean	std	min	25 %	50 %	75 %	max
fn-initial	1.275	0.078	1.023	1.222	1.274	1.328	1.571
nn-initial	0.410	0.044	0.243	0.381	0.410	0.439	0.634
fn-final	1.163	0.090	0.899	1.100	1.160	1.225	1.507
nn-final	0.296	0.042	0.136	0.268	0.295	0.323	0.479
initial-final	0.456	0.124	0.038	0.368	0.446	0.535	0.992



## 5 Configuration space dimensionality reduction

The application of various constraints confines the valid configurations to a region of the configuration space that potentially needs fewer dimensions to be described (rather than the full number of 21 dimensions of the original configuration space). Since the structure of this region is neither identified nor apparent, a dedicated method for identification of the corresponding dimensionality is needed. We are using the method presented in [6] which relies solely on the distances of the two nearest neighbors for each data point. This has the advantage that the bias due to curvature or density variations is reduced in the estimate.

Table 6 shows the resulting estimates for the three data sets. These indicate that further constraining the beta function along the beamline or at the target location, beyond the values of 500 m and 1 m, does not decrease the number of intrinsic dimensions. Hence we use the  $\mathcal{D}_{1,0}^{500}$  data set as a representative for the further analysis.

Table 6: Estimation of number of intrinsic dimensions for the different data sets.

data set	intrinsic dimension	
	initial	final
$\mathcal{D}_{1,0}^{500}$	16.23	12.93
$\mathcal{D}_{0,2}^{500}$	16.27	12.07
$\mathcal{D}_{1,0}^{250}$	16.05	12.62

## 6 Configuration space microstructure

The accuracy of the power supplies used in HEST is about 100 ppm and the precision is about 200 ppm. Therefore the total relative uncertainty of magnet current setting is about  $\delta = \Delta I/I = 3 \times 10^{-4}$  [10] which also applies to the relative uncertainty of each  $k_1$ -value. The potential difference between theoretical and actual setting in terms of distance in  $k_1$ -space depends on the  $k_1$ -values and has the following upper bound:

$$\Delta k_{1,tot} = \delta \cdot \sqrt{6 \cdot (\max |k_{1,QPK}|)^2 + 15 \cdot (\max |k_{1,QPL}|)^2} = 7.5 \times 10^{-4} \text{ m}^{-2} \quad (3)$$

In order to investigate the configuration space microstructure, for each configuration in data set  $\mathcal{D}_{1,0}^{500}$ , a set of 5000 additional configurations was generated inside the 21-dimensional ball with radius  $0.001 \text{ m}^{-2}$  around that original configuration. These additional configurations were filtered according to the matching constraints and those that fulfill the constraints, in the following called *leaf configurations*, are used for further analysis. These leaf configurations are the result of pure Monte Carlo sampling without any matching procedure. Hence they do not reflect any properties of the previously used LMDIF matching algorithm.

The distribution of the number of leaf configurations is shown on the left plot of Figure 7. The configuration space structure at this scale is very rich. In some areas the sampling method found no leaf configurations, what means that the original configuration is vulnerable to small errors in quadrupoles setting. On the other hand, there are a few areas which are filled with many leaf configurations and these areas are tolerant towards quadrupole errors.

An example of a region with a large number of good configurations is shown on right plot of Figure 7. The data for this plot was obtained using the above mentioned technique of probing the configuration space around each seed configuration in  $\mathcal{D}_{1.0}^{500}$ , with additional sampling of consecutive shells, each with the same thickness of  $0.001 \text{ m}^{-2}$  and containing 5000 samples, until no leaf configurations are found anymore. Since the volume of each shell increases with power 21, the intersection and thus the number of leaf configurations per shell, will decrease in case the probed region of potentially valid configurations locally spans less than 21 dimensions. This implies that even though the number of leaf configurations goes to zero, there is no evidence that the region of valid configurations is bounded at the same level in configuration space, just that the probability to sample a configuration in the intersection of that region with the hypershell decreases accordingly. Nevertheless the thus obtained data gives an idea about the spatial distribution of leaf configurations around particularly good seed configurations.

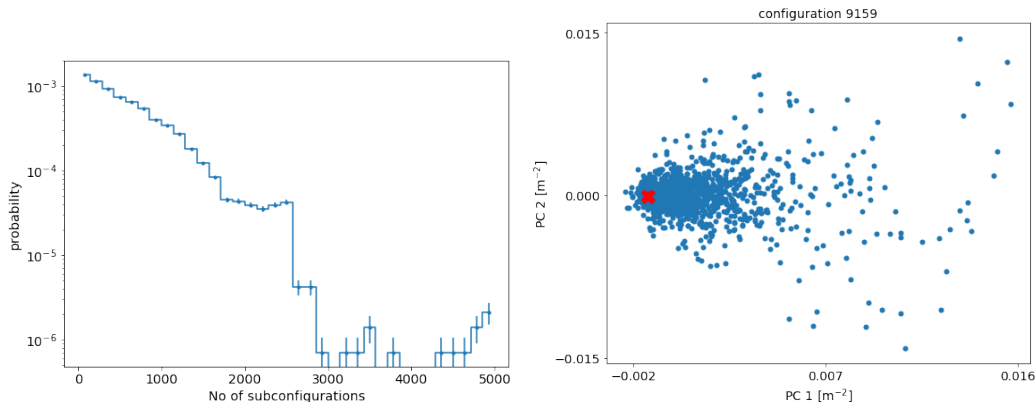


Figure 7: Left: Number of leaf configurations found within the 21-ball of radius  $0.001 \text{ m}^{-2}$  around each configuration in the data set  $\mathcal{D}_{1.0}^{500}$ . Right: Example of a distribution of leaf configurations corresponding to a particularly large region of valid configurations. The two-dimensional distribution is obtained by projecting onto the plane of largest variance (principal components). The seed configuration is marked with a red "x".

## 7 Principal Component Analysis

Principal component analysis allows to find the main degrees of freedom of the studied system and thus to potentially reduce dimensionality of the configuration space. The aspect of dimensionality reduction is useful for visualization and processing of high-dimensional data sets.

The optimal number of principal components can be found using method from [11]. The method, applied to the data set  $\mathcal{D}_{1,0}^{500}$ , shows that the first two components are responsible for about 30% of the total variance in the data and the remaining components vary significantly less, as illustrated in the left plot of Figure 8. Imposing a stronger constraint on target focusing makes the first two principal components more pronounced, i.e. responsible for a larger fraction of the total variance.

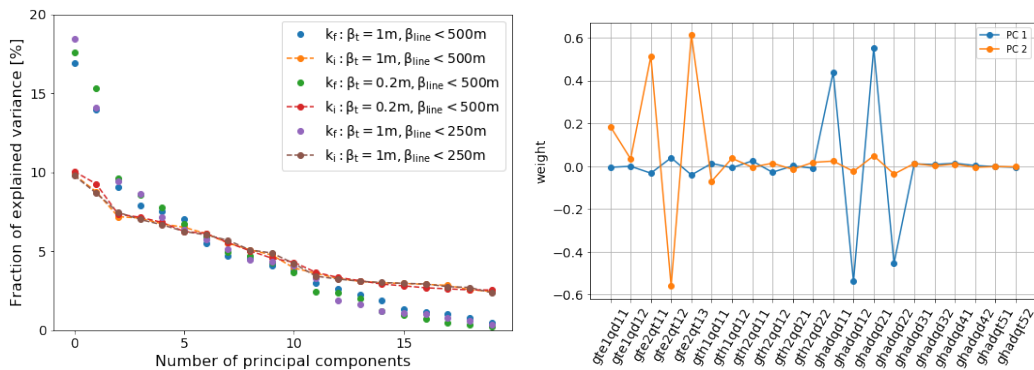


Figure 8: Left: Fraction of the variance in the data explained by the given principal components - the first two principal components explain about 30% of the variance. Right: Composition of the first two principal components for the  $\mathcal{D}_{1,0}^{500}$  data set (for other data sets similar results are obtained). The horizontal axis shows the name of the quadrupole magnet along the beamline and the vertical axis shows the weight associated with corresponding  $k_1$ -value.

The weights associated to the first and second principal components, here called PC1 and PC2, are shown on the right plot of Figure 8. The first principal component mainly consists of the contribution of the two quadrupole doublets GHADQD(11|12) and GHADQD(21|22) while the second component corresponds to the quadrupole triplet GTE2QT(11|12|13) at the beginning of the beamline.

In order to better understand the meaning of the principal components, the plots of Figure 9 shows the  $k_1$ - values of all quadrupole magnets for those configurations that expose extreme values of PC1 and PC2. Negative values of PC1 correspond to strong focusing in the GHADQD-zone and positive values of PC2 correspond to strong focusing in GTE2QT-zone.

The Figure 10 shows the mean value as well as standard deviation of the absolute  $k_1$ -values along the beamline. The final focusing magnets have large  $k_1$ -values but rather small spread of the values. The plot also shows the BEAMTIME2019 optics

configuration which is commonly used in daily operation.

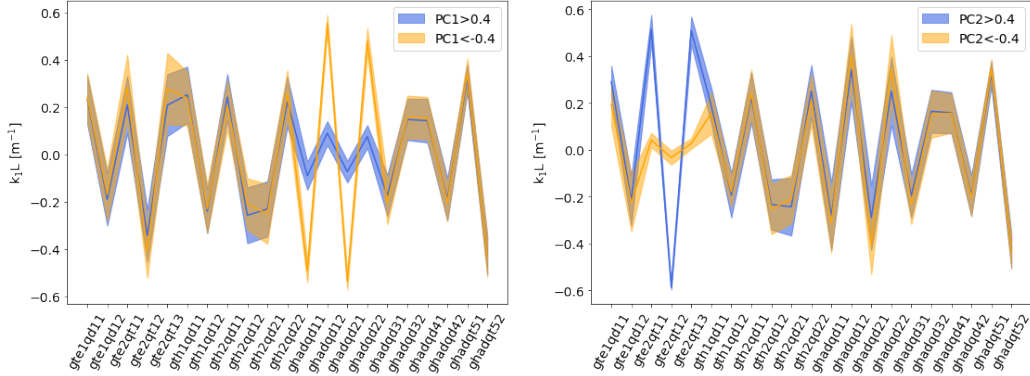


Figure 9: Visualization of configurations corresponding to large magnitudes of the first (left plot) and second (right plot) principal components.

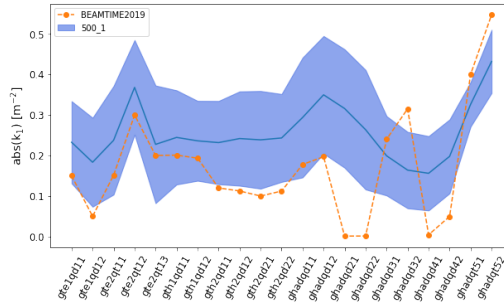


Figure 10: Mean and standard deviation of  $k_1$ -values along the beamline. The BEAMTIME2019 configuration, used in operation, is shown as well.

Figure 11 shows a density map of all configurations projected onto the plane corresponding to the first two principal components. This is referred to as *PC-space* in the following. The left plot shows a density map corresponding to initial  $k_1$ -values which were used as starting points for the matching procedure; only those values that could be successfully optimized are included. The right plot shows the corresponding  $k_1$ -values after the matching procedure converged. The models are spread, but clearly the preferred values are for small negative first and second principal components. More than 50% of the configurations lie in the area defined by  $-0.2 < PC1, PC2 < 0.0$ .

## 8 Clustering

The goal of clustering is to investigate if the optics configurations can be divided into groups of common features. Several algorithms were tested, but the only interesting results were obtained using the k-means algorithm. This algorithm performs

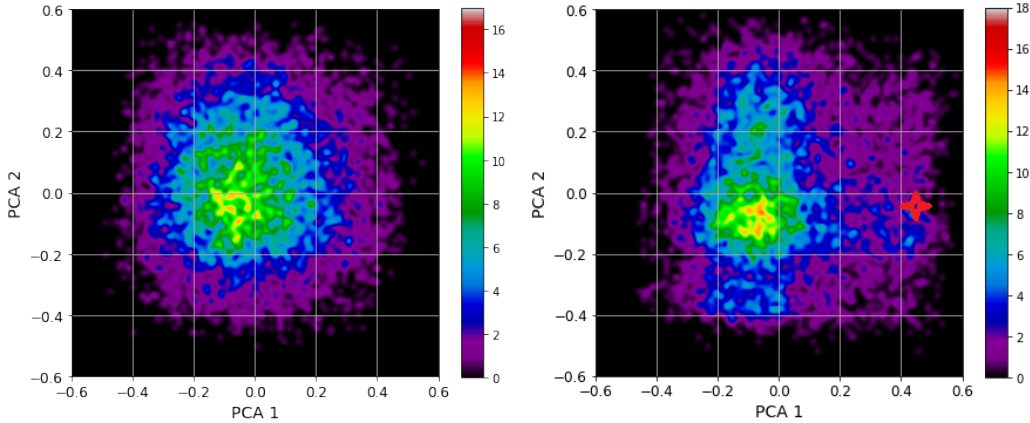


Figure 11: Density of models in  $PC$ -space for the initial (left plot)  $k_1$ -value settings and the ones after the matching procedure converged (right plot). The star on the right plot shows the position of ion optics settings currently used in operation (BEAMTIME2019, see Figure 1).

a partitioning of the data, that is it does not find an optimal number of clusters but it divides the data into a predefined number of partitions.

The elbow curve, shown on the left plot of Figure 12, can be used to estimate the optimal number of clusters. The choice of number of clusters is less straightforward than the choice of minimum number of Principal Components. Visually the number of three clusters seems to be a better choice than two or four. The subsequent results were obtained requesting three clusters.

The right plot of Figure 12 shows division of the PC component configuration space into 3 clusters. Those clusters are clearly distinguishable and contain respectively: 21%, 47% and 32% of configurations. If two clusters are requested, the partitioning reveals a clear distinction between negative and positive values of the second principal component (PC1), ie. configurations are split between strong and weak focus in GTE2QT segment. If more than three clusters are chosen, the resulting partitions overlap in the PC1-PC2 projection of the configuration space.

The clustering algorithm is applied in  $k_1$ -space, but the same results are obtained when it is applied in PC-space. It means that the features detected by the algorithm are present in the first two Principal Components and not in other components.

The left plot of Figure 13 presents the distribution of  $k_1$ -values and the horizontal optics functions for the three clusters. It is interesting to note that the unsupervised algorithm, which is k-means clustering, finds three main strategies for ion optics on the HADES beamline:

- cluster 0, with strong focus in GTE2QT segment,
- cluster 1, with weak focus in GTE2QT segment and strong focus in GHADQD segment,

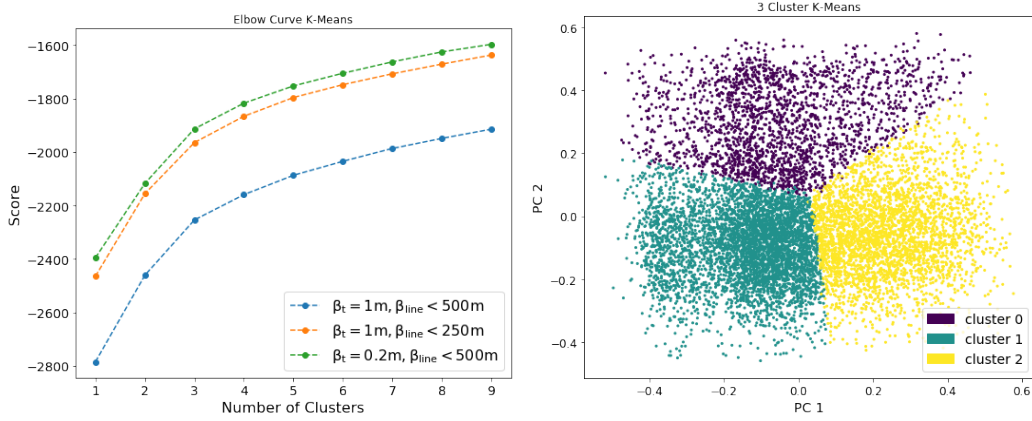


Figure 12: Left: elbow curve for k-means algorithm. Right: cluster coverage in principal component space.

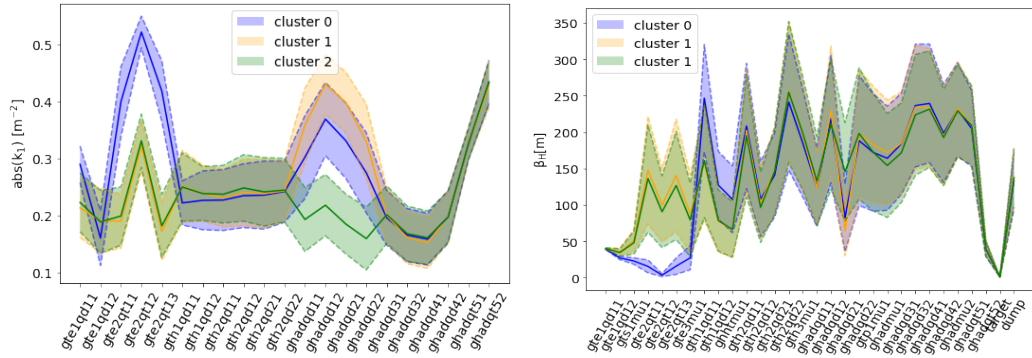


Figure 13: Left: the distribution of quadrupoles k-values along the beamline for 3-cluster analysis. For better visibility the absolute value of k-values is displayed. Right: horizontal beta function along the line for the three clusters. The line represents mean value and the band represent half of standard deviation.

- cluster 2, with weak focus in GTE2QT segment and weak focus in GHADQD segment.

## 9 Stability of optics configurations

The stability of an optics configuration can refer to two different aspects. One aspect is the change of the beta functions along the beamline and at the target location as a function of change of the Twiss parameters at the entrance of the beamline. Such a shifting of lattice parameters can lead to an increase of beam spot size at the target and hence it is desirable that a configuration is *robust* against such shifting.

The other aspect is concerned with quadrupole gradient errors. Small changes in the  $k_1$ -values might lead to an increase of the beam spot size at the target location

and hence it is desirable that a configurations is *tolerant* towards such gradient errors.

Here we define the *robustness* and *tolerance* of configurations as follows. The robustness score is given by the formula:

$$\text{Robustness} = \sqrt{\max\left(\frac{\Delta\beta_{h,\text{target}}}{\beta_{h,\text{target}}}, 0\right)^2 + \max\left(\frac{\Delta\beta_{v,\text{target}}}{\beta_{v,\text{target}}}, 0\right)^2} \quad (4)$$

The  $\Delta\beta_{(h,v),\text{target}}$  is the result of a shifting of the Twiss parameters at the entrance of the beamline. The max part ensures that only an increase in beta functions is taken into the account and hence a robustness score of zero indicates that the configuration is robust against the shifting, i.e. it will not increase the beta function at the target location. A robustness score greater than zero indicates an increase in beta function by a corresponding magnitude.

The tolerance of a configuration towards quadrupole gradient errors can be assessed via the number of valid configurations that are found in a ball with corresponding radius around that configuration. This is similar to the sampled leaf configurations from Section 6, where the distribution of tolerance is presented in Figure 7. Here we define the tolerance of a configuration as the fraction of leaf configurations:

$$\text{Tolerance} = \frac{N_{\text{leaves}}}{N_{\text{samples}}} \quad \text{within } R = 0.001 \text{ m}^{-2} \quad (5)$$

Figure 14 presents a particular and non-trivial property of optics configurations: the most tolerant configurations have the  $k_1$ -values of the two last focusing quadrupoles close to their average value. Therefore, in order to speed-up the search for high-tolerance configurations, one could restrict the  $k_1$ -values of these magnets.

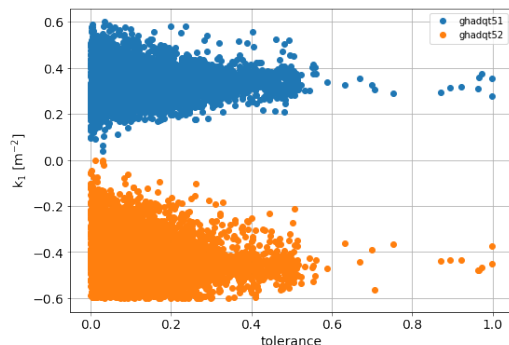


Figure 14: Strength of final focusing quadrupoles in function of tolerance.

The HADES experiment requires slowly extracted beams and the optics of the synchrotron change during the quadrupole-driven slow extraction process which causes the lattice parameters at the entrance of the transfer line to change too. According to dedicated optics calculations [12] the values of  $\beta_h$ ,  $\beta_v$  and horizontal dispersion  $D_h$  at the entrance of the beamline vary during the spill by 3%, 1% and

3.5% respectively. For the following analysis we recompute the beamline lattice functions with modified values at the entrance of the beamline and observe the change of beta function at the experimental target location for each of the configurations in the data set  $\mathcal{D}_{1.0}^{500}$ . The change of beta functions at the target location is denoted with  $\Delta\beta_h$  and  $\Delta\beta_v$ .

As the beamline lattice is mostly linear, the expected change of lattice parameters at the end of the line is of the same order of magnitude as the variation at the entrance of the beamline. The relative changes of beta functions at the target location are shown on the left plot of Figure 15.

The vertical change is about 30% of the horizontal one, as expected from the changes imposed at the entrance of the beamline and the fact that part of the beamline is tilted, therefore leading to coupling of the two planes.

The distribution has clear maxima - deviation of the optics function on the target is non-zero, however a small population of configurations lie in a wide minimum of the configuration space, where they seem quite independent on the variation of beam parameters at the beginning of the beamline.

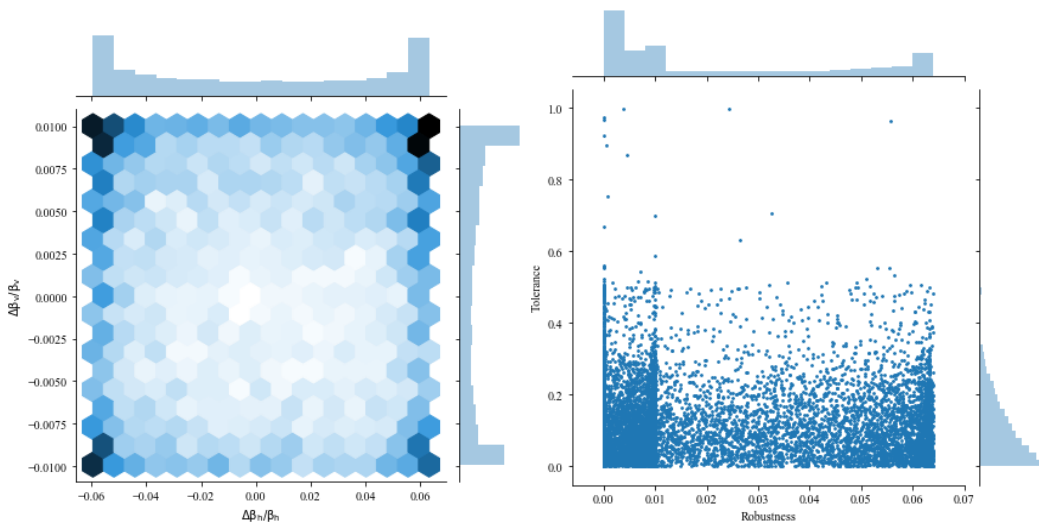


Figure 15: Relative change of the beta functions on experimental target due to variation of the beam parameters at the beginning of the beamline.

The results show that 22% of the models are robust against a shifting of the lattice functions with a few models leading even to a significant decrease of the beta function at the target location in both planes.

## 10 Ion optics choice

An interesting observation is that most of the historically used ion optics settings of the beamline are located in same region of PC-space, at about  $PC1 = (0.42, 0.44)$



and  $PC2 = (-0.05, 0.05)$  (see Figures 11, 17). In this region the focus of GHADQD magnets is weak and for GTE2QT magnets it is moderate (belonging to cluster 2).

As mentioned before, there is no single best solution for ion optics of a multi-purpose beamline. However, the configurations found in the exhaustive scan of the available configuration space reveal various levels of tolerance towards quadrupole errors, robustness with respect to shifting of lattice functions and are characterized by various levels of dispersion at the target location.

Two particular configurations have been investigated as a potential substitute for historically used settings. The first, no. 336, has a robustness score of zero (full robustness) and maximal tolerance. The second one, no. 5741, is chosen with similar criteria but selecting only from configurations which have very small horizontal dispersion on the target:  $D_x < 0.1$  m. These configurations are shown in Figures 16 and 17.

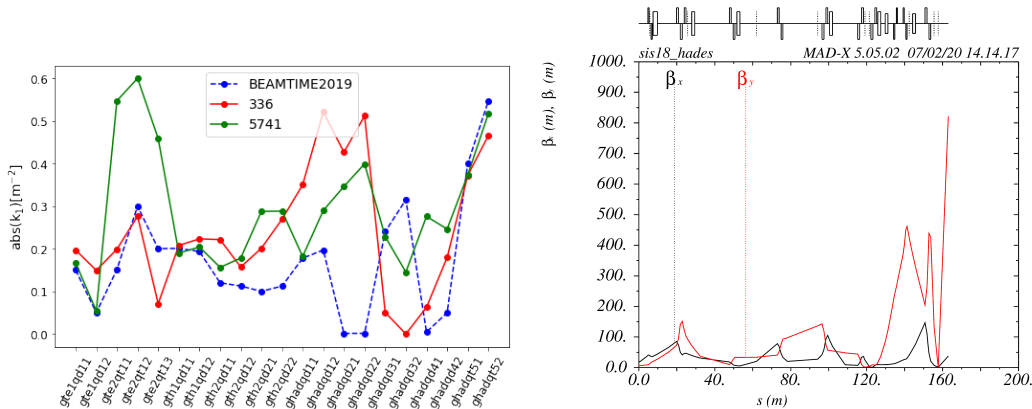


Figure 16: Left: comparison of  $k_1$ -values for operational ion optics settings with two new settings proposed as an outcome of the study. Right: optics functions for configuration #336.

Right plot of Figure 17 suggests that good configurations are spread across the  $PC$ -space, without any particular regularity or preferences.

## 11 Conclusions

The analyzed beamline is designed to be flexible as other beamlines bifurcate from it and the main experiment HADES, which is situated at the end of this line, operates in various modes. The methodology of the study relies on generation of large amounts of configurations spread in the available configuration space and by executing the matching procedure with constraints on focusing beam on the target and keeping beam envelope within the beamline acceptance.

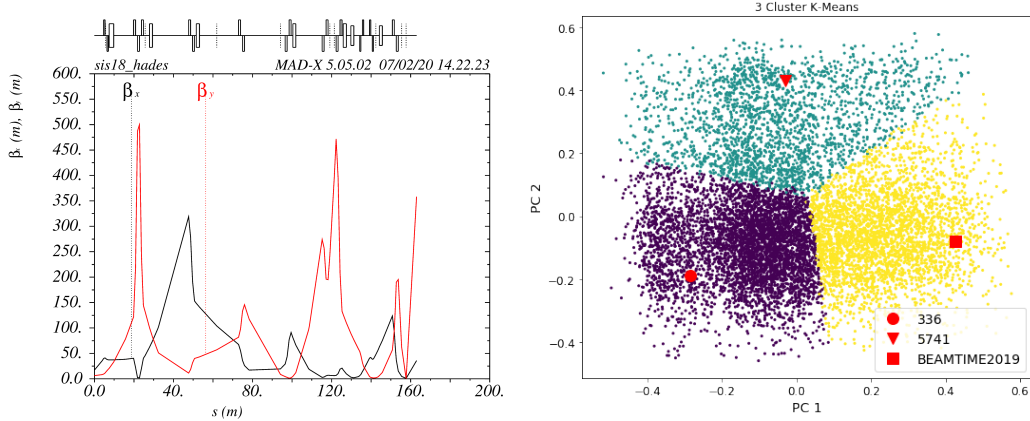


Figure 17: Left: optics functions for configuration #5741. Right: location of the discussed configurations in principal component space.

The following conclusions are the highlights of the study:

- When stronger constraints are imposed on the target focusing, more quadrupoles along the beamline are employed to meet the constraint, what is expressed by selection of particular values of a total phase advance.
- The configuration space of matched optics fills a small, but continuous region of the total possible configuration space.
- However, this region is not uniform: there are configurations which are tolerant to change of  $k_1$ -values and others which are not; This is expressed as a variation of density of matched configurations.
- Principal Component Analysis reveals that two beamline sections, one at the beginning and one in the middle have most variance while setting of other magnets is more constrained.
- Partitioning the available configurations shows that three approaches to construction of beamline optics can be distinguished, based on values of the first two Principal Components.
- Configurations have also varying tolerance to the change of the initial twiss parameters.
- Neither tolerance to varying initial twiss parameters nor robustness of the configurations were found to favour some particular region of configuration space.
- A choice of new optics configurations can be done based on selection of particularly robust and tolerant configurations.

The presented analysis allows for investigation of the possible ion optics settings of a beamline. It reveals what types of optics are possible and gives indications about sensitivity of the optics to various errors, like uncertainty of beam parameters at the entrance to the beamline or quadrupole errors.

In the future developments, it is planned to check other matching procedures, especially gradient-free ones and to perform more precise studies of configuration space microstructure.

## References

- [1] <http://sapinski.web.cern.ch/sapinski/physics/HEST/index.html>
- [2] G. Agakishiev et al., “The High-Acceptance Dielectron Spectrometer HADES”, *Eur.Phys.J. A41* (2009) 243-277
- [3] M. Sapinski, O. Geithner, C. Hessler, S. Reimann, P. Schtt, M. Vossberg and B. Walasek-Hhne, “Measurements of the GSI Transfer beamlines Ion Optics,” in *Proc. IPAC’19, Melbourne, Australia, May 2019*, doi:10.18429/JACoW-IPAC2019-MOPGW024
- [4] M. Sapinski et al. “Upgrade of GSI HADES beamline in Preparation for High Intensity Runs”, in *Proc. IPAC’17, Copenhagen, Denmark, May 2017*, pp.2214
- [5] A. Rost et al., “Performance of the CVD Diamond Based Beam Quality Monitoring System in the HADES Experiment at GSI”, in *Proc. IPAC’19, , Melbourne, Australia, May 2019*
- [6] Facco, E., dErrico, M., Rodriguez, A. et al. Estimating the intrinsic dimension of datasets by a minimal neighborhood information. *Sci Rep* 7, 12140 (2017)
- [7] <http://madx.web.cern.ch/madx/>, version 5.04.02
- [8] [http://en.wikipedia.org/wiki/Levenberg-Marquardt\\_algorithm](http://en.wikipedia.org/wiki/Levenberg-Marquardt_algorithm)
- [9] <https://scikit-learn.org/>
- [10] A. Stafiniak, priv. comm.
- [11] T.P. Minka, Automatic choice of dimensionality for PCA, in *NIPS, Vol. 13*, pp. 598-604 (2000).
- [12] S. Sorge, priv. comm.